Preprint version. This manuscript has not yet been reviewed.

Supporting Information for

High-Pressure Deformation of Iron–Nickel–Silicon Alloys and Implications for Earth's Inner Core

Matthew C. Brennan[1], Rebecca A. Fischer[1], Samantha Couper[2], Lowell Miyagi[2], Daniele Antonangeli[3], Guillaume Morard[4]

[1]Department of Earth and Planetary Sciences, Harvard University

[2]Department of Geology and Geophysics, University of Utah

[3]IMPMC, Sorbonne Université

[4]ISTerre, Université Grenoble Alpes

Contents of this file

Text S1
Figures S1–S2
Tables S1–S2
References

Text S1.

The following equations were used to calculate the alloy properties plotted in Figure 6 of the main text. All equations are functions of differential stress τ. Modified from Gleason and Mao (2013), Reaman et al. (2011), and references therein. Parameter values are listed in Table S1.

Dislocation velocity: $$v = \left(\frac{V_D a' b L}{w^2}\right) \exp\left(\frac{-\Delta H_0}{kT}\right) \sinh\left(\Delta H_0 - \frac{\Delta H}{kT}\right) \quad \text{(S1)}$$

Activation enthalpy: $$\Delta H = \Delta H_0 \left[1 - \left(\frac{\tau_p}{\tau}\right)^{3/4}\right]^{4/3} \quad \text{(S2)}$$

Strain rate: $$\dot{\epsilon} = b v \left(\frac{\tau}{G_0 b}\right)^2 \quad \text{(S3)}$$

Critical grain size: $$d = \sqrt{\frac{A_{Dif}}{A_{Dis}} \frac{V}{b} \frac{k}{R} \ln\left(\frac{\alpha G}{2S\tau}\right) \left(\frac{G}{\tau}\right)^n} \quad \text{(S4)}$$

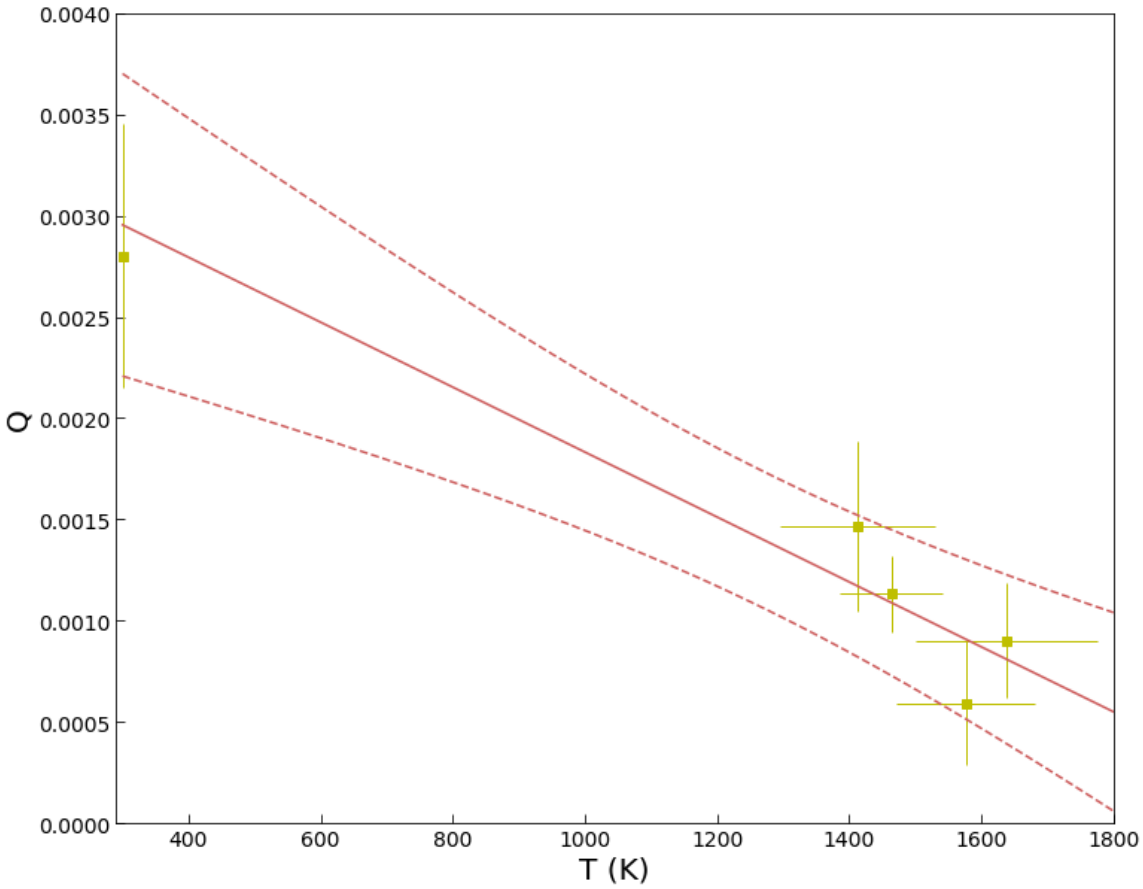

Figure S1.

Observed change of Q upon laser heating of Fe–5Si. The 300 K point (upper left) was calculated from the Fe–5Si fit (main text Figure 3). High temperature data are from consecutive diffraction images collected at approximately the same pressure (43–46 GPa; see main text Figure 2). Dashed lines are 95% confidence intervals.

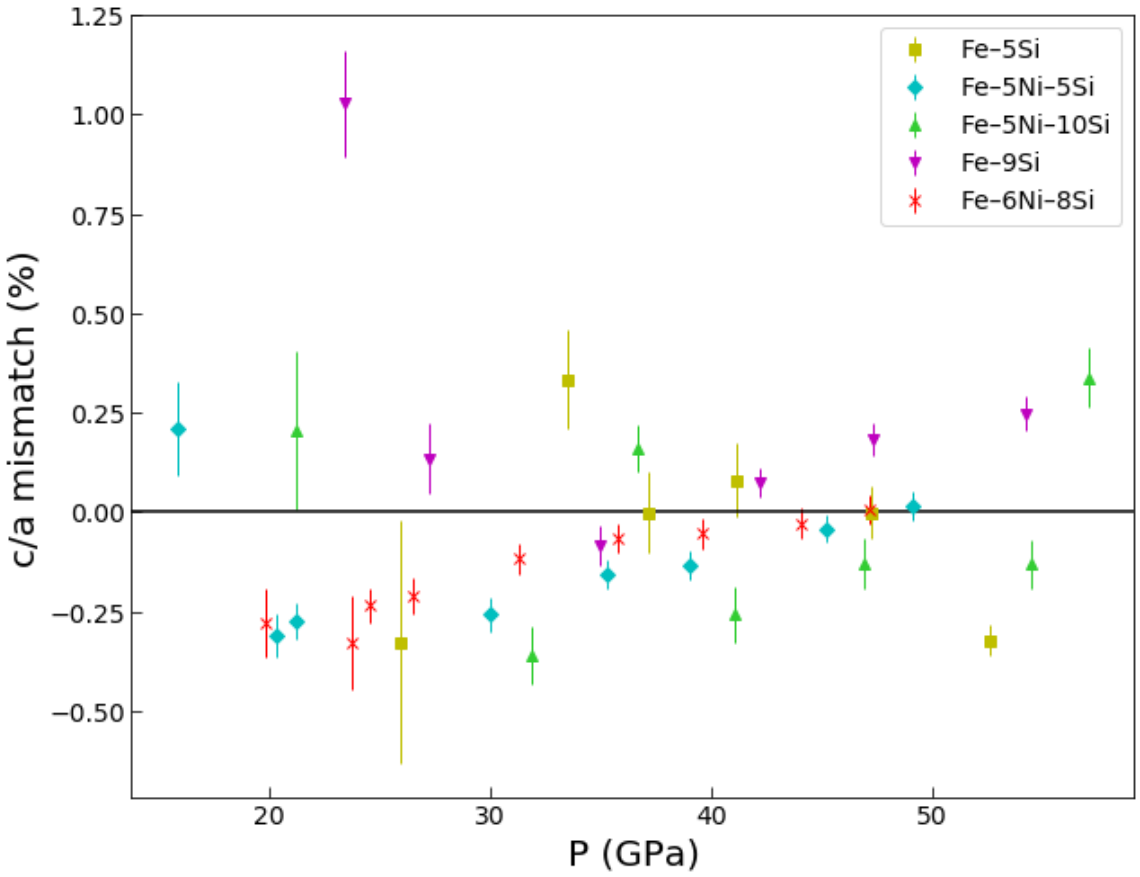

Figure S2.

Comparison between our experimentally-determined ratio of hcp unit cell parameters (i.e., the ratio of c-axis length and a-axis length) and the ratio calculated using the parametrization of Fischer and Campbell (2015). 'Mismatch' here is defined as $\left(\frac{\text{measured } c/a - \text{calculated } c/a}{\text{calculated } c/a}\right) \times 100$. Despite the nonhydrostatic conditions of our radial diffraction experiments, the measured and calculated unit cell ratios agree quite well at 300 K.

composition	phases	*T* (K)	*P* (GPa)	hcp *c* (Å)	hcp *a* (Å)	Q
Fe–5Si	bcc	300	12.6(35)	-	-	-
Fe–5Si	bcc–hcp	300	19.9(36)	3.9538(11)	2.454(4)	0.00151(16)
Fe–5Si	bcc–hcp	300	23.7(26)	3.9425(8)	2.449(9)	0.00153(10)
Fe–5Si	hcp	300	24.6(29)	3.9345(5)	2.442(2)	0.00222(6)
Fe–5Si	hcp	300	26.5(39)	3.9229(6)	2.435(2)	0.00278(7)
Fe–5Si	hcp	300	31.3(26)	3.9074(5)	2.425(2)	0.00299(5)
Fe–5Si	hcp	300	35.8(24)	3.8881(5)	2.413(2)	0.00321(5)
Fe–5Si	hcp	300	39.6(29)	3.8645(5)	2.399(2)	0.00334(6)
Fe–5Si	hcp	300	44.0(56)	3.8551(5)	2.393(2)	0.00315(6)
Fe–5Si	hcp	300	47.1(29)	3.8472(4)	2.388(2)	0.00315(5)
Fe–5Si	hcp*	300	45.4(26)	3.8486(4)	2.389(2)	0.00303(5)
Fe–5Si	hcp*	300	44.3(20)	3.8533(4)	2.392(2)	0.00261(5)
Fe–5Si	hcp*	300	38.0(46)	3.8592(4)	2.396(5)	0.00222(5)
Fe–5Si	hcp*	300	35.5(38)	3.8722(4)	2.404(2)	0.00247(4)
Fe–5Ni–5Si	bcc	300	6.5(14)	-	-	-
Fe–5Ni–5Si	bcc–hcp	300	15.9(14)	3.9812(16)	2.456(5)	0.00194(27)
Fe–5Ni–5Si	bcc–hcp	300	20.4(19)	3.9445(7)	2.448(2)	0.00240(7)
Fe–5Ni–5Si	hcp	300	21.2(24)	3.9295(6)	2.439(2)	0.00302(6)
Fe–5Ni–5Si	hcp	300	30.0(10)	3.9108(5)	2.428(2)	0.00327(7)
Fe–5Ni–5Si	hcp	300	35.3(14)	3.8880(5)	2.413(2)	0.00329(6)
Fe–5Ni–5Si	hcp	300	39.1(14)	3.8722(4)	2.404(2)	0.00354(5)
Fe–5Ni–5Si	hcp	300	45.2(14)	3.8514(4)	2.390(1)	0.00361(5)
Fe–5Ni–5Si	hcp	300	49.1(34)	3.8333(4)	2.379(2)	0.00360(5)
Fe–5Ni–5Si	hcp*	300	48.7(17)	3.8330(9)	2.380(3)	0.00284(10)
Fe–5Ni–5Si	hcp*	300	48.1(14)	3.8356(5)	2.382(2)	0.00206(6)
Fe–5Ni–5Si	hcp*	300	39.7(7)	3.8592(12)	2.397(3)	0.00198(6)
Fe–5Ni–10Si	bcc	300	11.7(40)	-	-	-
Fe–5Ni–10Si	bcc–hcp	300	25.9(34)	3.9249(44)	2.432(10)	0.00143(33)
Fe–5Ni–10Si	bcc–hcp	300	33.5(12)	3.9155(17)	2.412(5)	0.00158(22)
Fe–5Ni–10Si	hcp	300	37.2(12)	3.8821(13)	2.401(4)	0.00236(14)
Fe–5Ni–10Si	hcp	300	41.2(13)	3.8708(12)	2.393(4)	0.00278(14)
Fe–5Ni–10Si	hcp	300	47.2(18)	3.8514(8)	2.384(3)	0.00320(13)
Fe–5Ni–10Si	hcp	300	52.6(18)	3.8271(5)	2.377(2)	0.00346(10)
Fe–5Ni–10Si	hcp*	300	50.5(15)	3.8449(7)	2.376(2)	0.00276(10)
Fe–5Ni–10Si	hcp*	300	47.1(43)	3.8577(7)	2.385(3)	0.00166(9)
Fe–5Ni–10Si	hcp*	300	40.7(45)	3.8783(3)	2.399(9)	0.00172(10)
Fe–6Ni–8Si	bcc	300	6.8(14)	-	-	-
Fe–6Ni–8Si	bcc–hcp	300	21.3(12)	3.9693(29)	2.449(7)	0.00292(27)
Fe–6Ni–8Si	bcc–hcp	300	31.9(13)	3.9154(10)	2.432(3)	0.00331(12)
Fe–6Ni–8Si	hcp	300	41.0(15)	3.8917(9)	2.416(3)	0.00447(20)
Fe–6Ni–8Si	hcp	300	36.7(11)	3.9169(8)	2.421(2)	0.00444(10)

composition	phases	*T* (K)	*P* (GPa)	hcp *c* (Å)	hcp *a* (Å)	Q
Fe–6Ni–8Si	hcp	300	46.9(14)	3.8673(8)	2.400(3)	0.00505(12)
Fe–6Ni–8Si	hcp	300	54.5(16)	3.8452(8)	2.387(2)	0.00564(12)
Fe–6Ni–8Si	hcp	300	57.1(20)	3.8456(10)	2.377(3)	0.00576(11)
Fe–6Ni–8Si	hcp*	300	55.9(13)	3.8468(7)	2.382(2)	0.00533(9)
Fe–6Ni–8Si	hcp*	300	50.1(17)	3.8570(7)	2.392(2)	0.00371(9)
Fe–6Ni–8Si	hcp*	300	44.5(15)	3.8699(10)	2.400(3)	0.00348(14)
Fe–9Si	bcc	300	7.6(6)	-	-	-
Fe–9Si	bcc–hcp	300	23.5(7)	3.9800(19)	2.435(5)	0.00280(37)
Fe–9Si	bcc–hcp	300	27.3(7)	3.9336(19)	2.429(3)	0.00209(17)
Fe–9Si	hcp	300	35.0(7)	3.8934(6)	2.412(2)	0.00339(8)
Fe–9Si	hcp	300	42.2(7)	3.8714(5)	2.396(1)	0.00398(6)
Fe–9Si	hcp	300	47.3(8)	3.8555(5)	2.385(2)	0.00453(7)
Fe–9Si	hcp	300	54.2(9)	3.8334(6)	2.371(2)	0.00506(8)
Fe–9Si	hcp*	300	52.4(8)	3.8361(4)	2.374(1)	0.00385(5)
Fe–9Si	hcp*	300	48.4(20)	3.8446(21)	2.382(6)	0.00263(28)
Fe–9Si	hcp*	300	39.4(7)	3.8798(5)	2.400(1)	0.00078(9)
Fe–5Si	hcp–fcc	1577(105)	43.1(8)	3.8992(4)	2.410(4)	0.00059(31)
Fe–5Si	hcp–fcc	1638(138)	44.4(10)	3.8948(4)	2.410(8)	0.00090(28)
Fe–5Si	hcp–fcc	1412(117)	45.4(9)	3.8802(10)	2.406(4)	0.00147(42)
Fe–5Si	hcp–fcc	1463(78)	44.5(7)	3.8808(18)	2.408(6)	0.00113(19)

Table S1.

Data from our radial diffraction experiments. All data were collected at Advanced Light Source beamline 12.2.2 (Kunz et al., 2005). Asterisks indicate diffraction images taken during sample decompression. Compositions are in weight percent. Q is the average of all observed sample peaks (see main text for details). Numbers in parentheses are uncertainties on the last digit(s). Pressures were calculated from the equation of state of Pt (Fei et al., 2007) at 300 K or MgO (Speziale et al., 2001) at high temperatures. Temperature measurement is described in Kunz et al. (2018).

Parameter		Value	Source
Debye frequency	V_D	13 THz	Gleason and Mao (2013)
Peierls barrier width	a'	0.2 nm	Gleason and Mao (2013)
Burgers vector	b	0.5 nm	Gleason and Mao (2013)
Kink pair width	w	20 nm	Gleason and Mao (2013)
Dislocation length	L	500 nm	Gleason and Mao (2013)
Standard activation enthalpy	ΔH_0	6 eV	Gleason and Mao (2013)
Peierls stress	τ_p	varies	This study
Aggregate shear modulus	G	varies	This study; Gleason and Mao (2013); Regan et al. (2018)
Ambient aggregate shear modulus	G_0	varies	This study; Gleason and Mao (2013); Regan et al. (2018)
Geometrical constant of diffusion	A_{Dif}	30	Reaman et al. (2011)
Geometrical constant of dislocation	A_{Dis}	1.8	Reaman et al. (2011)
Schmid factor constant	$\alpha/_{2S}$	0.6	Reaman et al. (2011)
Power-law constant	n	2	Reaman et al. (2011)
Specific volume	V	varies	Dewaele et al. (2006); Fischer et al. (2014)

Table S2.

Parameters used in Equations S1–S4. We retain the values used in previous studies, except for Peierls stress, which we set equal to our recalculated strength (main text Figure 5), and specific volume, which we recalculated for the alloy compositions used (assuming that the effect of Ni is negligible).

References

Dewaele, A., Loubeyre, P., Occelli, F., Mezouar, M., Dorogokupets, P. I., & Torrent, M. (2006). Quasihydrostatic equation of state of Iron above 2 Mbar. *Physical Review Letters*, *97*(21), 215504. doi: 10.1103/PhysRevLett.97.215504

Fei, Y., Ricolleau, A., Frank, M., Mibe, K., Shen, G., & Prakapenka, V. (2007). Toward an internally consistent pressure scale. *Proceedings of the National Academy of Sciences*, *104*(22), 9182–9186.

Fischer, R. A., & Campbell, A. J. (2015). The axial ratio of hcp Fe and Fe-Ni-Si alloys to the conditions of Earth's inner core. *American Mineralogist*, *100*(11–12), 2718–2724. doi: 10.2138/am-2015-5191

Fischer, R. A., Campbell, A. J., Caracas, R., Reaman, D. M., Heinz, D. L., Dera, P., & Prakapenka, V. B. (2014). Equations of state in the Fe-FeSi system at high pressures and temperatures. *Journal of Geophysical Research: Solid Earth*, *119*(4), 2810–2827. doi: 10.1002/2013JB010898

Gleason, A. E., & Mao, W. L. (2013). Strength of iron at core pressures and evidence for a weak Earth's inner core. *Nature Geoscience*, *6*(7), 571–574. doi: 10.1038/ngeo1808

Kunz, M., MacDowell, A. A., Caldwell, W. A., Cambie, D., Celestre, R. S., Domning, E. E., et al. (2005). A beamline for high-pressure studies at the Advanced Light Source with a superconducting bending magnet as the source. *Journal of Synchrotron Radiation*, *12*(5), 650–658. doi: 10.1107/S0909049505020959

Kunz, M., Yan, J., Cornell, E., Domning, E. E., Yen, C. E., Doran, A., et al. (2018). Implementation and application of the peak scaling method for temperature measurement in the laser heated diamond anvil cell. *Review of Scientific Instruments*, *89*(8), 083903. doi: 10.1063/1.5028276

Reaman, D. M., Daehn, G. S., & Panero, W. R. (2011). Predictive mechanism for anisotropy development in the Earth's inner core. *Earth and Planetary Science Letters*, *312*(3–4), 437–442. doi: 10.1016/j.epsl.2011.10.038

Speziale, S., Zha, C.-S., Duffy, T. S., Hemley, R. J., & Mao, H. (2001). Quasi-hydrostatic compression of magnesium oxide to 52 GPa: Implications for the pressure-volume-temperature equation of state. *Journal of Geophysical Research: Solid Earth*, *106*(B1), 515–528. doi: 10.1029/2000jb900318